Relationship between structural and dielectric properties of Znsubstituted Ba5CaTi2–xZnxNb8O30 tetragonal tungsten bronze

Amine Bendahhou, Pascal Marchet, Ablouh El-Houssaine, Soufian El Barkany, Mohamed Abou-Salama

Relationship between structural and dielectric properties of Zn-substituted $Ba_5CaTi_{2-x}Zn_xNb_8O_{30}$ tetragonal tungsten bronze

Amine bendahhou[1*], Pascal Marchet[2], Ablouh El-Houssaine[3], Soufian El Barkany[1], Mohamed Abou-Salama[1]

[1] *Laboratory of Molecular Chemistry, Materials and Environment, Department of Chemistry, Faculty Multidisciplinary Nador, University Mohamed Premier, B.P. 300, Selouane, Nador 62700, Morocco*

[2] *IRCER – UMR CNRS 7315, Université de Limoges, Centre Européen de la Céramique, 12 Rue Atlantis, F-87068 Limoges Cedex, France*

[3] *Laboratory of Bioorganic and Macromolecular Chemistry, Department of Chemistry, Faculty of Sciences and Technologies, Cadi Ayyad University, 40000 Marrakesh, Morocco*

* corresponding author. Tel : +212606849738

E-mail address : bendahhou_amine1718@ump.ac.ma (A. Bendahhou)

Abstract

$Ba_5CaTi_{2-x}Zn_xNb_8O_{30}$ ceramics with (x=0, 0.04, and 0.08) were synthesized by conventional solid-state reaction method at 1300°C for 6 hours. The effects of the Ti/Zn ratio on structural and dielectric properties were studied by changing the value of x. The pure phase formation of all prepared $Ba_5CaTi_{2-x}Zn_xNb_8O_{30}$ compositions was confirmed by X-ray diffraction. The refinement of the (XRD) data by the Rietveld method confirmed the tetragonal crystal structure with the space group P4bm at room temperature. Scanning electron microscopy (SEM) of $Ba_5CaTi_{2-x}Zn_xNb_8O_{30}$ ceramics shows good sinterability, low porosity and uniform distribution of grains of unequal size over the entire surface in all samples. The average grain size is in the range of 1.3 to 1.6 μm. The frequency-dependent dielectric properties were examined by complex impedance spectroscopy in the temperature range of 50°C to 420°C where a structural phase transition was observed for all samples.

Keywords: Tetragonal tungsten bronze; Ceramics; Solid state reaction; X-ray diffraction; Structure; Phase transition; Dielectric properties.

1. Introduction

Lead-free materials have an important place in electronics due to technological progress, the toxicity of lead and the desire to protect the environment [1-3]. Tetragonal tungsten bronzes (TTBs) are materials derived from the perovskite structure which, due to their polyvalent structure, can have very important and advantageous electrical, magnetic, catalytic, optical or

photocatalytic properties, with diverse applications in the electronics, chemical and energy conversion sectors [4-8]. Recently, tungsten bronze compounds had been considered as one of the candidates to replacing lead compounds [9, 10]. An TTB cell is composed of 10 deformed BO_6 octahedrons, linked by their summits and forming three types of sites, which are square A1, pentagonal A2 and triangular C. This structure can therefore be represented by the formula $[(A1)_2(A2)_4(C)_4][(B1)_2(B2)_8]O_{30}$ [11, 12]. The sites A1, A2 and C or the center of the oxygen octahedron can be occupied by different cations [13-17]. In our study, the smallest site C is vacant and their general formula thus becomes $[(A1)_2(A2)_4][(B1)_2(B2)_8]O_{30}$. The variety of cationic sites (A1, A2, C, B1, and B2) gives rise to a great variety of structures, allowing the improvement of the characteristics of TTBs, by substitutions in A1 and A2 sites or in B1 and B2 octahedrons.

From the dielectric point of view, ferroelectric compounds are divided into two groups: conventional ferroelectrics and relaxors [18]. In recent years, research on TTB ceramics has concentrated on the influence of A-site substitution on their phase structure and dielectric properties. Concerning the effects of doping ions, most papers focused on the effect of substitution of A sites by the rare earth, alkali and alkaline earths metal. Yang et al has been suggested that alkali metal ions can increase the Curie temperature [19]. $Ba_{4-x}Sr_xSmFe_{0.5}Nb_{9.5}O_{30}$ compounds have been considered as relaxors, and it is the disorder of the Ba/Sr cations in the A sites that results in the creation of strong dielectric relaxation [20]. Zhu et al [21-23] reported that, for ferroelectric $M_4R_2Ti_3Nb_7O_{30}$ (M=Ba, Sr; R=rare earth) of tungsten bronze, the difference in radius between the cations at the A1 and A2 sites could significantly affect the dielectric properties. Research on $Ba_{4-x}Sr_xDy_{0.67}Nb_{10}O_{30}$ (x = 0, 0.25, 0.5, 1, 2, 3) ceramics found that the compounds are normal ferroelectric for x = 1, while they are relaxors ferroelectric when x = 2, and Tc decreases with the increase in amount of Sr [24]. Stennett et al reported an increase in the Curie temperature with the decrease in ion radius M at site A1 in the filled TTB, $Ba_2MTi_2Nb_3O_{15}$ (M = Bi, La, Pr, Nd, Sm, Eu, Gd and Dy), with a transition between normal ferroelectric (M = Pr, Nd, Sm, Eu, Gd and Dy) to relaxor ferroelectric (M = Bi and La) behavior [25, 26]. Although in most perovskite structures, B-site substitution can lead to a relaxor transition [27] and improve dielectric permittivity [28], suggesting that B-site substitution is an excellent method of enhancing dielectric properties of tetragonal tungsten bronze.

The present work is focused on titanium-zinc substitution for compounds of general composition $Ba_5CaTi_{2-x}Zn_xNb_8O_{30}$ (x=0, 0.04, and 0.08) synthesized by standard solid-state reaction. The aims of the present work are: (i) to study the structural modifications resulting

from Zn substitution, (ii) to investigate the dielectric properties of ceramic samples (relative permittivity, dielectric losses) as a function of Zn content in order to understand the relationships between structure and dielectric properties of $Ba_5CaTi_{2-x}Zn_xNb_8O_{30}$ ceramics.

2. Materials and methods

$Ba_5CaTi_{2-x}Zn_xNb_8O_{30}$ ceramics with (x=0, 0.04, and 0.08) were prepared by the conventional solid-state reaction method. The raw materials used were $BaCO_3$ (Sigma-Aldrich 99%), $CaCO_3$ (Aldrich 99.9%), Nb_2O_5 (Aldrich 99.9%), ZnO (Himedia 99.9%) and TiO_2 (Sigma-Aldrich 99%). The raw materials were weighed in stoichiometric quantities according to the reaction below and mixed by ball-milling in ethanol for 4 hours using zirconia balls. The mixed powders were dried at 80 °C, homogenized in an agate mortar for 30 minutes and calcined at 1300°C for 6 hours.

$$5BaCO_3 + CaCO_3 + (2-x)TiO_2 + xZnO + 4Nb_2O_5 \rightarrow Ba_5CaTi_{2-x}Zn_xNb_8O_{30} + 6CO_2$$

The obtained powders were ground and mixed with polyvinyl alcohol (PVA) as a binder. Then, cylindrical pellets were obtained by pressing at 20 kN (12 mm diameter, 2 mm thickness). The green pellets were sintered at 1450°C for 6 hours in air. The temperature was first raised to 1100°C at a rate of 10°C/min and then reached the sintering temperature with a rate of 5°C/min. Finally, the samples were naturally cooled to room temperature.

The identification of the crystalline structure of the powders was performed by X-ray diffraction (XRD) using CuKα radiation (λ=1.5406 Å) at room temperature (293 K, 0.015° step, 10 - 120° 2θ range, scanning speed of 1°/min). The lattice parameters, atomic positions, occupation rate, and thermal agitation factor were refined by the Rietveld method using the Jana 2006 software [29]. The average crystallite size "D" was estimated for the strongest diffraction peak using the Scherrer equation [30]. The sintered pellet was polished with a fine emery paper to make both surfaces flat and parallel and then annealed at 1300°C for 30 min. The microstructure of $Ba_5CaTi_{2-x}Zn_xNb_8O_{30}$ ceramics was checked by scanning electron microscopy (SEM) (TESCAN VEGA III LM), with an accelerating voltage of 10kV. The average grain size of ceramic samples was estimated using Image J software. Before electrical measurements, the sintered ceramic was painted with silver paste and annealed for 30 minutes at 300°C to adhere to the silver on the sample and then cooled to room temperature before taking any measurement. The disc shaped silver coated pellet behaves like a parallel plate capacitor which is used for dielectric measurements. The relative permittivity, and dielectric losses (tan δ) were determined using a

BioLogic impedance analyzer (MTZ-35) over the frequency range of 1 kHz to 1 M Hz, the furnace and the sample temperatures were controlled by MT-lab software using a heat-up rate of 5 °C/min.

3. Results and discussion

3.1. Structural study

The X-ray diffraction (XRD) patterns of $Ba_5CaTi_{2-x}Zn_xNb_8O_{30}$ ceramics with (x=0, 0.04, and 0.08) recorded at room temperature in the range 2θ varies between 10-80° with different x values are shown in Fig.1 All samples have a tetragonal tungsten bronze structure (TTB) and no second phase can be detected, indicating that Zn^{2+} has diffused into the bronze structure to form a solid solution in which Zn^{2+} occupies the sites (B1 and B2) of the TTB structure.

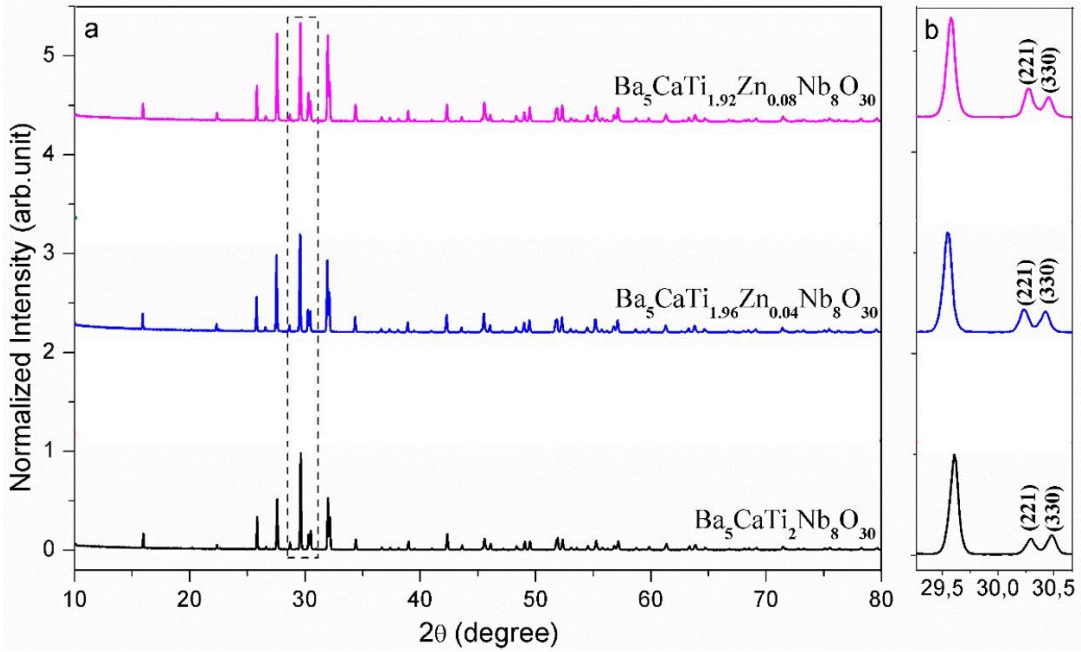

Fig. 1. XRD diffraction diagrams of $Ba_5CaTi_{2-x}Zn_xNb_8O_{30}$ powders calcined at 1300 ° C as a function of x (a); (b) the magnification of (a) in the range of 20 ° to 35 °

To confirm the effect of Zinc on the crystal structure, magnified XRD spectra are shown in Fig. 1(b). According to Fig. 1(b), two peaks divided into about 30.4° are peaks (221) and (330), respectively. As the Zn^{2+} concentration increases, the intensity of peak (221) gradually increases to become identical to peak (330) at x=0.04 and then the intensity of peak (221) increases with increasing Zn content, suggesting that some distortion of the crystal structure appears when Zn^{2+} is introduced into (B1 and B2) sites.

Table 1. Experimental parameters for X-ray powder diffraction of $Ba_5CaTi_{2-x}Zn_xNb_8O_{30}$ (x=0, 0.04, and 0.08).

Chemical formula	$Ba_5CaTi_2Nb_8O_{30}$	$Ba_5CaTi_{1.96}Zn_{0.04}Nb_8O_{30}$	$Ba_5CaTi_{1.92}Zn_{0.08}Nb_8O_{30}$
a (Å)	12.4614(6)	12.4667(5)	12.4672(6)
b (Å)	12.4614(6)	12.4667(5)	12.4672(6)
c (Å)	3.98366(19)	3.98510(16)	3.98406(19)
V ($Å^3$)	618.61(5)	619.36(4)	619.24(5)
D (μm)	0.894	0.818	0.812
Space group	P4bm	P4bm	P4bm
Symmetry	Tetragonal	Tetragonal	Tetragonal
Rp (%)	6.04	5.77	6.33
Rwp (%)	8.10	7.65	8.55
GOF	1.58	1.39	1.67

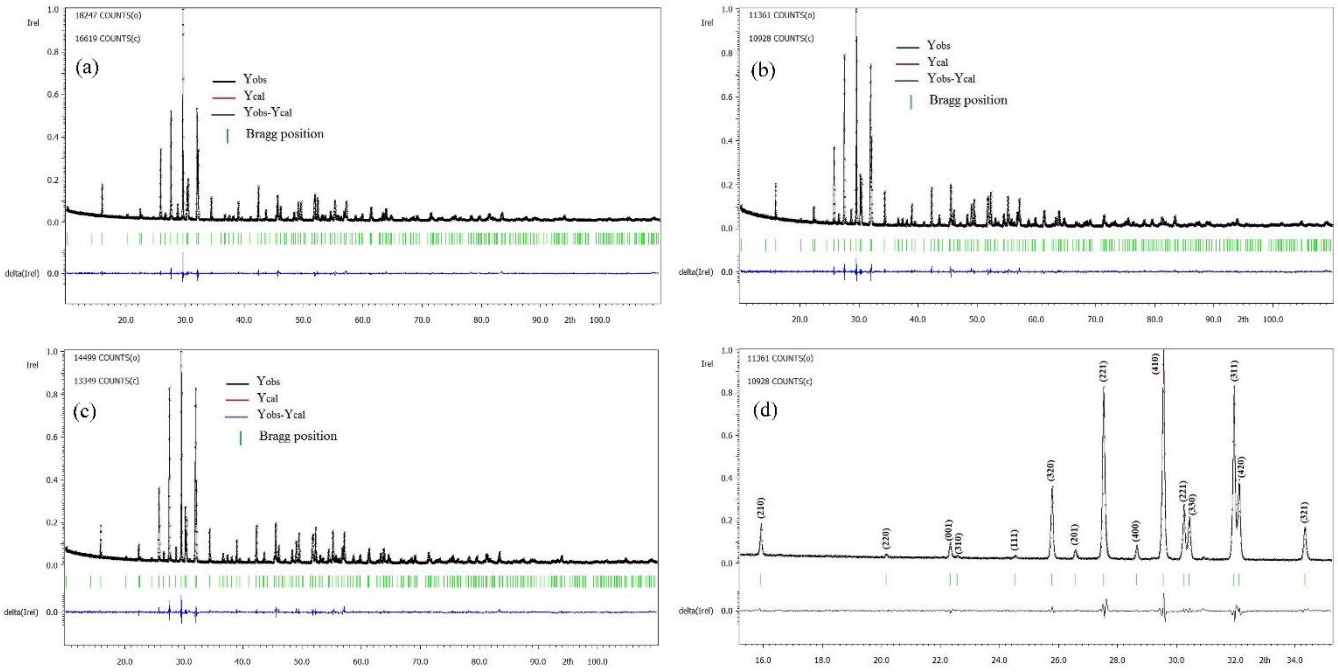

Fig. 2. X-ray diffraction refinements for powder $Ba_5CaTi_{2-x}ZnxNb_8O_{30}$: (a) x= 0, (b)x= 0.04, and (c)x= 0.08 and (d) the magnification of (b) in the range of 20 ° to 35°.

We refined the X-ray diffraction spectra and found that all samples were single-phase with the non-centrosymmetric P4bm space group (Fig. 2), where Ba^{2+} sit in the A2 site (the pentagonal site), the residue of the Ba^{2+} with the Ca^{2+} occupy the A1 site (the square site) simultaneously with a ratio of 1:1, while Ti^{4+}, Zn^{2+} and Nb^{5+} occupying the B site with a ratio of 2-x:x:8.

Fig. 2(d) shows the magnification of Fig. 2(b) in the range 15° to 35° to illustrate the quality of refinement in the P4bm space group. All diffraction peaks (hkl) are indexed, their intensity and shape being satisfactorily reproduced using the refined parameters. The adjustment between the experimental and calculated models is relatively good, and the reliability factors are comparatively high (see Table. 1), but the quality of the refinements is sufficient to discuss the proposed structural model and investigate the structural parameters in more detail.

The refined cell parameters, and the reliability factors are presented in Table 1. The refined structural parameters (atomic positions, thermal agitation factor, and occupation rate) are given in Table 2. Tables 3 and 5 provide the selected bond distances and bond angles, respectively. Fig. 3 represents the crystallographic structure along the c-axis for the composition $Ba_5CaTi_{1.92}Zn_{0.08}Nb_8O_{30}$. In the tungsten-bronze structure, two types of octahedrons with different environments are signed as B1 and B2 (see Fig. 3); the interstices A1 (tetragonal) are surrounded by four B2 octahedrons, the interstices A2 (pentagonal) are surrounded by four B2 octahedrons and one B1 octahedron.

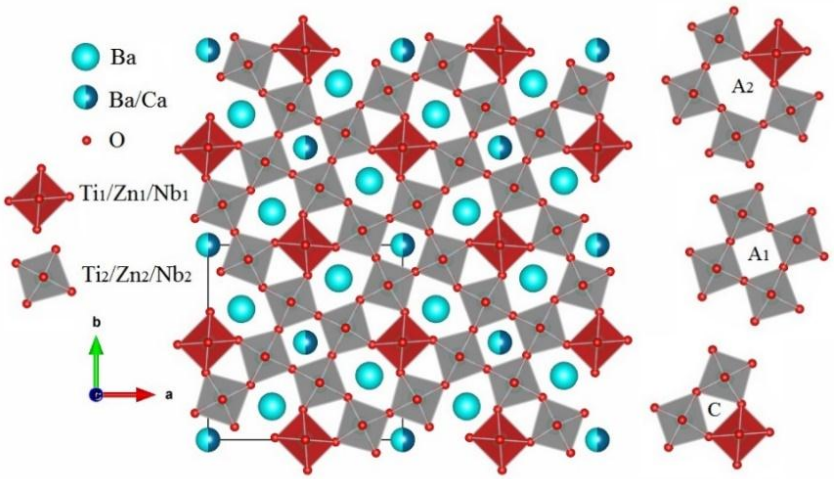

Fig. 3. Representation of the TTB structure of $Ba_5CaTi_{1.92}Zn_{0.08}Nb_8O_{30}$ along the "c" axis.

Table 2. Refinement structural parameters for $Ba_5CaTi_{2-x}Zn_xNb_8O_{30}$ with (x=0, 0.04, and 0.08).

Compound	Atom	Wyckoff position	x	y	c	Biso ($Å^2$)	Occupies
x= 0	Ca1/Ba1	2a	0	0	0	3.00(0)	0.501/0.499
	Ba2	4c	0.17142(7)	0.67142(7)	0	2.94(7)	0.993
	Ti1/Nb1	2b	0	0.50	0.505(2)	2.42(10)	0.2/0.8
	Ti2/Nb2	8d	0.07357(9)	0.21321(8)	0.503(2)	1.70(7)	0.2/0.8
	O1	2b	0	0.50	-0.045(10)	1.97(21)	0.9968
	O2	4c	0.2848(5)	0.7848(5)	0.460(8)	2.52(16)	0.9833
	O3	8d	0.0707(5)	0.2071(5)	-0.046(5)	2.52(16)	1.079
	O4	8d	0.3475(6)	0.0053(5)	0.435(4)	2.52(16)	0.996
	O5	8d	0.1383(6)	0.0682(6)	0.436(5)	2.52(16)	0.927
x= 0.04	Ca1/Ba1	2a	0	0	0	1.06(11)	0.549/0.451
	Ba2	4c	0.17139(7)	0.67139(7)	0	2.18(7)	1.001
	Ti1/Zn1/Nb1	2b	0	0.50	0.494(2)	1.66(10)	0.196/0.004/0.8
	Ti2/Zn2/Nb2	8d	0.07423(10)	0.21351(9)	0.498(2)	1.02(7)	0.196/0.004/0.8
	O1	2b	0	0.50	0.070(7)	1.44(19)	0.9982
	O2	4c	0.2887(5)	0.7887(5)	0.543(8)	1.44(19)	0.99
	O3	8d	0.0728(6)	0.2055(5)	0.043(5)	1.44(19)	1.030
	O4	8d	0.3424(7)	0.0075(5)	0.550(5)	1.44(19)	0.993
	O5	8d	0.1372(6)	0.0695(6)	0.566(4)	1.44(19)	0.973
x= 0.08	Ca1/Ba1	2a	0	0	0	1.54(11)	0.529/0.471
	Ba2	4c	0.17117(8)	0.67117(8)	0	2.63(8)	1.004
	Ti1/Zn1/Nb1	2b	0	0.50	0.499(3)	2.15(11)	0.192/0.008/0.8
	Ti2/Zn2/Nb2	8d	0.07412(11)	0.2139(10)	0.498(2)	1.47(8)	0.192/0.008/0.8
	O1	2b	0	0.50	0.044(11)	1.47(19)	0.9655
	O2	4c	0.2866(6)	0.7866(6)	0.538(9)	1.47(19)	0.9888
	O3	8d	0.0734(6)	0.2047(6)	0.036(7)	1.47(19)	0.979
	O4	8d	0.3421(7)	0.0054(5)	0.551(5)	1.47(19)	1.022
	O5	8d	0.1363(6)	0.0699(6)	0.565(4)	1.47(19)	1.000

The final chemical formula of $Ba_5CaTi_{2-x}Zn_xNb_8O_{30}$ with (x=0, 0.04, and 0.08) after the structural refinement step were respectively $Ba_{4.975}Ca_{0.997}Ti_2Nb_8O_{29.943}$,

$Ba_{4.906}Ca_{1.099}Ti_{1.96}Zn_{0.04}Nb_8O_{29.933}$, and $Ba_{4.96}Ca_{1.057}Ti_{1.92}Zn_{0.08}Nb_8O_{29.891}$ evidencing oxygen vacancies, this is attributed to the increase in the number of positive charges lost during the substitution of titanium by zinc and due to high sintering temperature (1450°C).

Table 3. Selected bond distance (Å) for $Ba_5CaTi_{2-x}Zn_xNb_8O_{30}$.

Bond Distances (Å)	x= 0	x= 0.04	x= 0.08
Ca(1)/Ba(1)-O(3)	2.733(6) × 4	2.723(7) × 4	2.714(7) × 4
Ca(1)/Ba(1)-O(5)	2.591(14) × 4	2.581(12) × 4	2.579(13) × 4
	2.955(15) × 4	2.961(13) × 4	2.952(14) × 4
<Ca(1)/Ba(1)-O>	2.759	2.755	2.748
Ba(2)-O(2)	2.71(2) × 1	2.76(2) × 1	2.75(3) × 1
	2.94(2) × 1	2.99(2) × 1	2.96(3) × 1
Ba(2)-O(4)	2.710(11) × 2	2.724(13) × 2	2.737(13) × 2
	3.068(12) × 2	3.003(14) × 2	3.020(14) × 2
Ti(1)/Zn(1)/Nb(1)-O(1)	1.79(4) × 1	1.69(3) × 1	1.81(4) × 1
	2.19(4) × 1	2.29(3) × 1	2.17(4) × 1
Ti(1)/Zn(1)/Nb(1)-O(4)	1.922(8) × 4	1.980(9) × 4	1.981(9) × 4
< Ti(1)/Zn(1)/Nb(1)-O >	1.944	1.983	1.984
Ti(2)/Zn(2)/Nb(2)-O(2)	1.985(7) × 1	1.957(7) × 1	1.965(8) × 1
Ti(2)/Zn(2)/Nb(2)-O(3)	1.80(2) × 1	1.81(2) × 1	1.84(3) × 1
	2.19(2) × 1	2.18(2) × 1	2.15(3) × 1
Ti(2)/Zn(2)/Nb(2)-O(4)	1.960(8) ×1	1.914(8) ×1	1.893(8) ×1
Ti(2)/Zn(2)/Nb(2)-O(5)	1.996(8) ×1	1.979(8) ×1	1.974(8) ×1
	2.016(8) ×1	2.047(8) ×1	2.057(8) ×1
< Ti(2)/Zn(2)/Nb(2)-O >	1.991	1.981	1.979

From table 3, we can see that Ca(1)/Ba(1)-O and Ti/Zn/Nb(2)-O distances decrease with increasing zinc content, but the substitution of Titanium by Zinc in the B1 octahedral sites causes an increase in the average Ti/Zn/Nb(1)-O distances. This observation suggests that the distribution of metal cations between the B1 and B2 octahedral sites is capable of changing the binding distances in solid solution $Ba_5CaTi_{2-x}Zn_xNb_8O_{30}$.

For all compositions, the cations Ti, Zn and Nb present clearly off-center displacements along the c-axis in both Ti/Zn/Nb(1)O_6 and Ti/Zn/Nb(2)O_6 octahedra (Fig. 4). The Ti/Zn/Nb(1)O_6

octahedra in all compositions have 180° O(1)–Ti/Zn/Nb(1)–O(1) bond angle (see Table 5) and four equal Ti/Zn/Nb(1)–O(4) bond length (see Table 3). In addition, the unequal Ti/Zn/Nb(2)–O bonds length of Ti/Zn/Nb(2)O_6 shows the displacement of the cations Ti/Zn/Nb(2) in the ab plane, and no displacement of the cations Ti/Zn/Nb(1) occurs in the ab plane indicating higher distortion in the octahedron Ti/Zn/Nb(2)O_6 than in Ti/Zn/Nb(1)O_6, which is demonstrated in the polyhedral representations in Fig. 6.

From Table 4 the off-center displacement of the Ti/Zn/Nb(2) cations in the ab plane increases with increasing zinc content in the $Ba_5CaTi_{2-x}Zn_xNb_8O_{30}$, suggesting that octahedral distortions also vary with increasing zinc content.

Table 4. The off-center displacement (Å) of the Ti/Zn/Nb(1) and Ti/Zn/Nb(2) cations.

	x=0	x=0.04	x=0.08
Ti/Zn/Nb(1) (c-axis)	0.41	0.62	0.36
Ti/Zn/Nb(2) (a-axis)	0.031	0.09	0.092
Ti/Zn/Nb(2) (b-axis)	0.036	0.065	0.081
Ti/Zn/Nb(2) (c-axis)	0.39	0.37	0.31

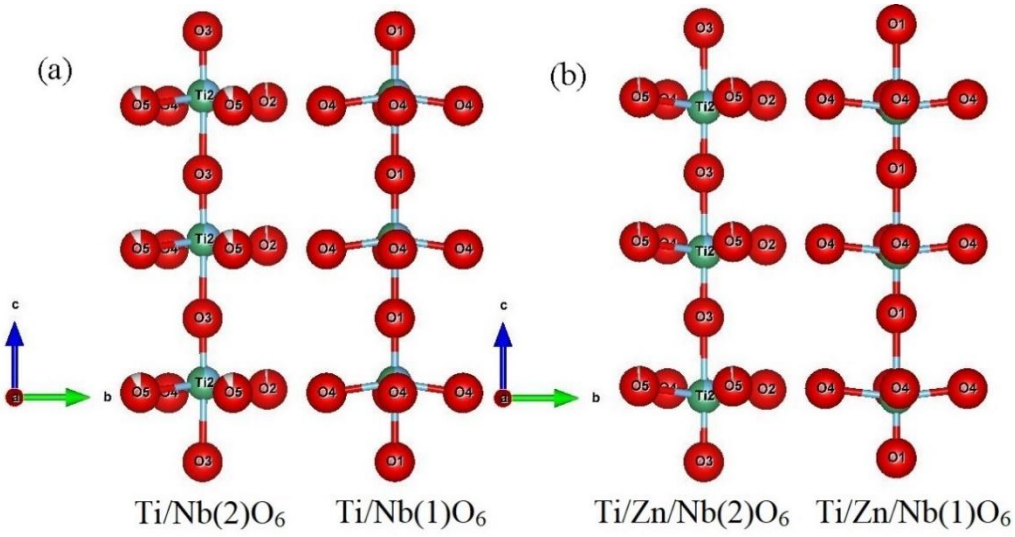

Fig. 4. Representations describing the distortions of the two kinds of octahedra in $Ba_5CaTi_{2-x}Zn_xNb_8O_{30}$; (a) x = 0, and (b) x= 0.04 along a axis.

The compression or dilation effects of the different octahedral cation-oxygen bonds can be described by the normalized bond length (the ratio of the actual to the ideal bond length). The

ideal bond length is calculated as the sum of the ionic radii of each cation-anion bond. The ion radii of the cations Ti, Nb and Zn in coordination 6 are 0.605 Å, 0.64 Å and 0.74 Å respectively. Any bond with a normalized value >1 is elongated otherwise is compressed.

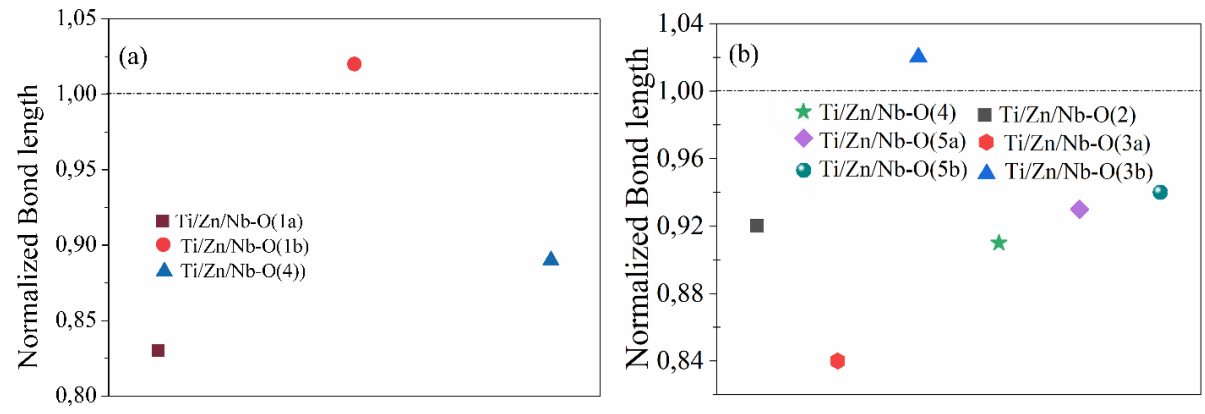

Fig. 5. Compression and dilatation effects of the corresponding selected bonds: normalized bond length of (a) Ti/Zn/Nb(1)-O ; (b) Ti/Zn/Nb(2)-O for $Ba_5CaTi_{1.96}Zn_{0.04}Nb_8O_{30}$ ceramic.

From Fig. 5 the Ti/Zn/Nb(1)O_6 octahedron, in all compositions, one of the Ti/Zn/Nb(1)-O(1) bonds is elongated and the other is compressed, indicating the off-center displacement of the Ti/Zn/Nb(1) along the c-axis (see Fig. 4), while the Ti/Zn/Nb(1)-O(4) bonds in the ab plane are compressed, which corresponds to the compression of the octahedrons of Ti/Zn/Nb(1)O_6 along the c axis, the displacement of the Ti/Zn/Nb(1) cations along the c axis is more important in compositions with x=0.04 (see Table 4). For the Ti/Zn/Nb(2)O_6 octahedron, in the ab plane, all four bonds are compressed, while along the c axis one of the Ti/Zn/Nb(2)-O(3) bonds is elongated and the other is compressed. The displacement of the Ti/Zn/Nb(2) cations along the c-axis decreases with increasing zinc content (see Table 4).

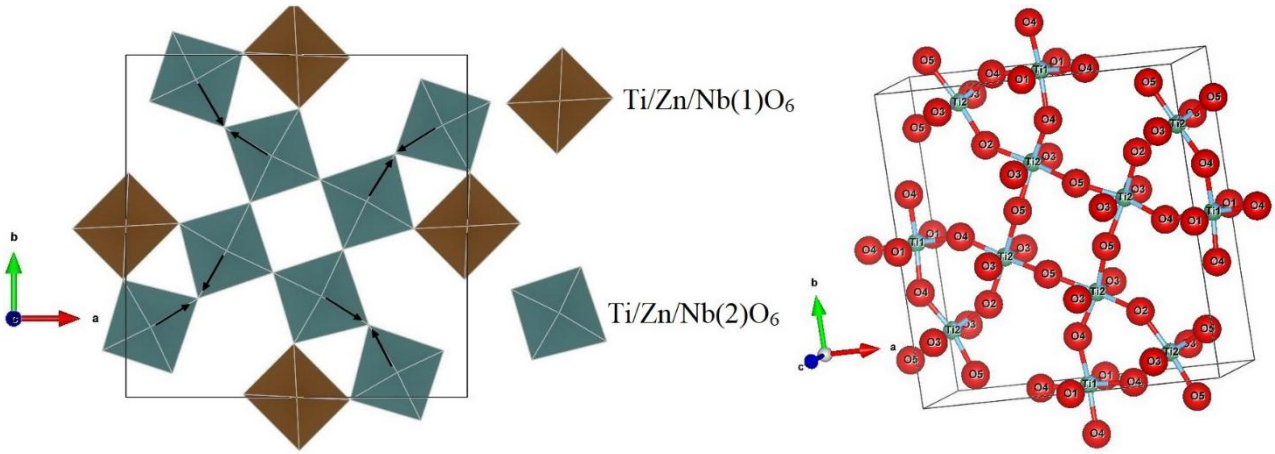

Fig. 6. Polyhedral representation of the tetragonal tungsten bronze $Ba_5CaTi_{1.96}Zn_{0.04}Nb_8O_{30}$ ceramics.

Depending on the polyhedral representations, the four oxygen ions of the octahedrons Ti/Zn/Nb(2)O_6 in the ab plane are gradually directed to different planes with increasing Zn content, which causes to tilting of the octahedrons Ti/Zn/Nb(2)O_6.

The arrows in Fig. 6 indicate the tilting direction of the octahedrons Ti/Zn/Nb(2)O_6. The Fig. 7 shows the angle of tilting of the octahedrons Ti/Zn/Nb(2)O_6 as a function of the content of Zn incorporated in $Ba_5CaTi_{2-x}Zn_xNb_8O_{30}$.

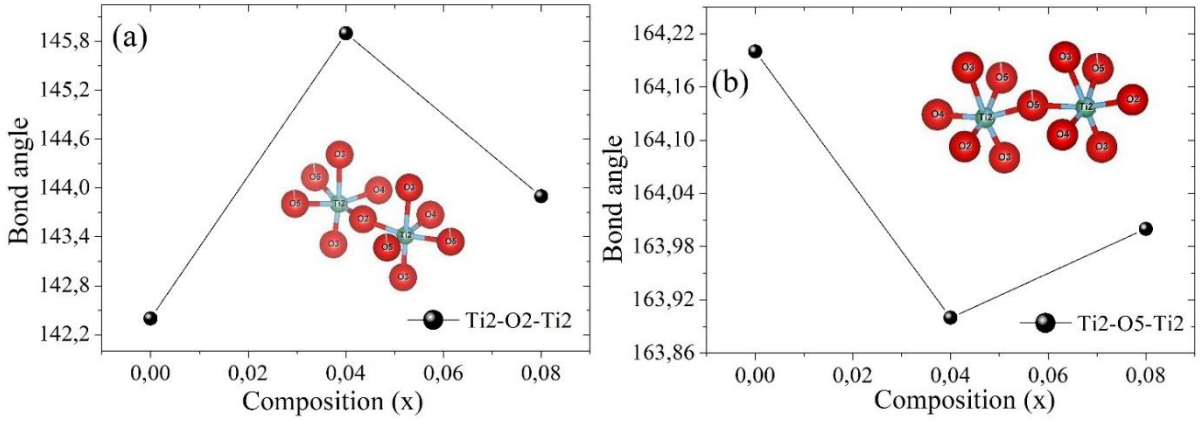

Fig. 7. The octahedral angles: (a) Ti(2)–O(2)–Ti(2), (b) Ti(2)–O(5)–Ti(2) as x increases.

Table 5. Selected bond angles for $Ba_5CaTi_{2-x}Zn_xNb_8O_{30}$.

Bond Angles (°)	x= 0	x= 0.04	x= 0.08
O(1)- Ti(1)/Zn(1)/Nb(1)-O(1)	180.0(5)	180.0(5)	180.0(5)
O(1)- Ti(1)/Zn(1)/Nb(1)-O(4)	81.6(5) × 4	83.5(6) × 4	83.9(6) × 4
	98.4(5) × 4	96.5(6) × 4	96.1(6) × 4
O(4)- Ti(1)/Zn(1)/Nb(1)-O(4)	84.9(3) × 2	83.9(3) × 2	85.5(3) × 2
	92.6(3) × 2	94.6(3) × 2	93.2(3) × 2
	163.2(9) × 2	166.9(9) × 2	167.9(10) × 2
O(2)- Ti(2)/Zn(2)/Nb(2)-O(3)	86.8(10)	86.4(10)	87.0(11)
	97.1(10)	97.3(10)	96.5(11)
O(2)- Ti(2)/Zn(2)/Nb(2)-O(4)	92.8(3)	93.0(3)	93.7(3)
O(2)- Ti(2)/Zn(2)/Nb(2)-O(5)	92.1(3)	94.3(3)	93.5(4)
	167.4(12)	167.0(11)	167.8(13)

O(3)- Ti(2)/Zn(2)/Nb(2)-O(3)	175.1(3)	174.1(3)	173.3(3)
O(3)- Ti(2)/Zn(2)/Nb(2)-O(4)	83.3(5)	85.7(6)	86.0(7)
	99.5(6)	98.7(6)	99.4(7)
O(3)- Ti(2)/Zn(2)/Nb(2)-O(5)	80.7(6)	79.8(6)	79.5(6)
	80.9(6)	80.7(5)	80.9(6)
	95.4(6)	95.3(6)	94.7(6)
	95.9(6)	95.7(6)	95.5(6)
O(4)- Ti(2)/Zn(2)/Nb(2)-O(5)	86.5(3)	84.8(3)	85.7(3)
	163.2(8)	163.3(8)	163.4(8)
O(5)- Ti(2)/Zn(2)/Nb(2)-O(5)	85.3(3)	84.6(3)	84.1(3)

3.2. Density and microstructure of $Ba_5CaTi_{2-x}Zn_xNb_8O_{30}$ ceramics

The relative density (ρ_r) of $Ba_5CaTi_{2-x}Zn_xNb_8O_{30}$ ceramics was obtained with the help of the following equation [20, 30]:

$$\rho_r = \rho_m/\rho_t$$

The relative density ρ_r is the ratio of measured density ($\rho_m = m/v$) and the theoretical density ($\rho_t = ZM/V_0N_A$), where m, v, M, V_o and N_A are the mass of pellet, volume of pellet, molar mass, volume of unit cell and Avogadro's constant.

The densities of $Ba_5CaTi_{2-x}Zn_xNb_8O_{30}$ ceramics are presented in Table 6. The relative densities for $Ba_5CaTi_{2-x}Zn_xNb_8O_{30}$ ceramics are 95.8%, 97.2%, and 97.0% respectively, suggesting that all samples are highly densified.

Table 6: The theoretical, calculated and relative densities of $Ba_5CaTi_{2-x}Zn_xNb_8O_{30}$ ceramics

Composition (x)	ρ_m (g/cm^3)	ρ_t (g/cm^3)	ρ_r (%)
0.0	5.262	5.490	95.8
0.04	5.330	5.484	97.2
0.08	5.326	5.489	97.0

SEM pictures of the surface of $Ba_5CaTi_{2-x}Zn_xNb_8O_{30}$ pellets sintered at 1450°C for 6 hours are shown in Fig. 8, with the results of grain size analysis. The microstructural characteristics depend on the transport mechanism of matter between grains via grain boundaries during the

sintering process. The absence of voids indicates that the samples have a high density and low porosity, in agreement with the measured relative densities. Grains of unequal size seem to be homogeneously distributed in all samples. It was seen that the large grains with an asymmetrical distribution of sizes could be due to the different movement kinetics across the boundaries [31]. After the sintering process was finished, the gain enhancement process was intensified, resulting in a reduction of pores and the disappearance of the smaller grains [32].

The histograms of Fig. 8 suggest that the average grain sizes for $Ba_5CaTi_{2-x}Zn_xNb_8O_{30}$ (x=0, 0.04 and 0.08) are respectively 1.31, 1.49 and 1.58 μm. These average values are slightly higher than the "D" values calculated by the Scherrer method. As a matter of fact, on one hand, this method gives only rough values. On another hand, the calculated values correspond to the size of the coherent diffracting domains, which is different from the true grain size.

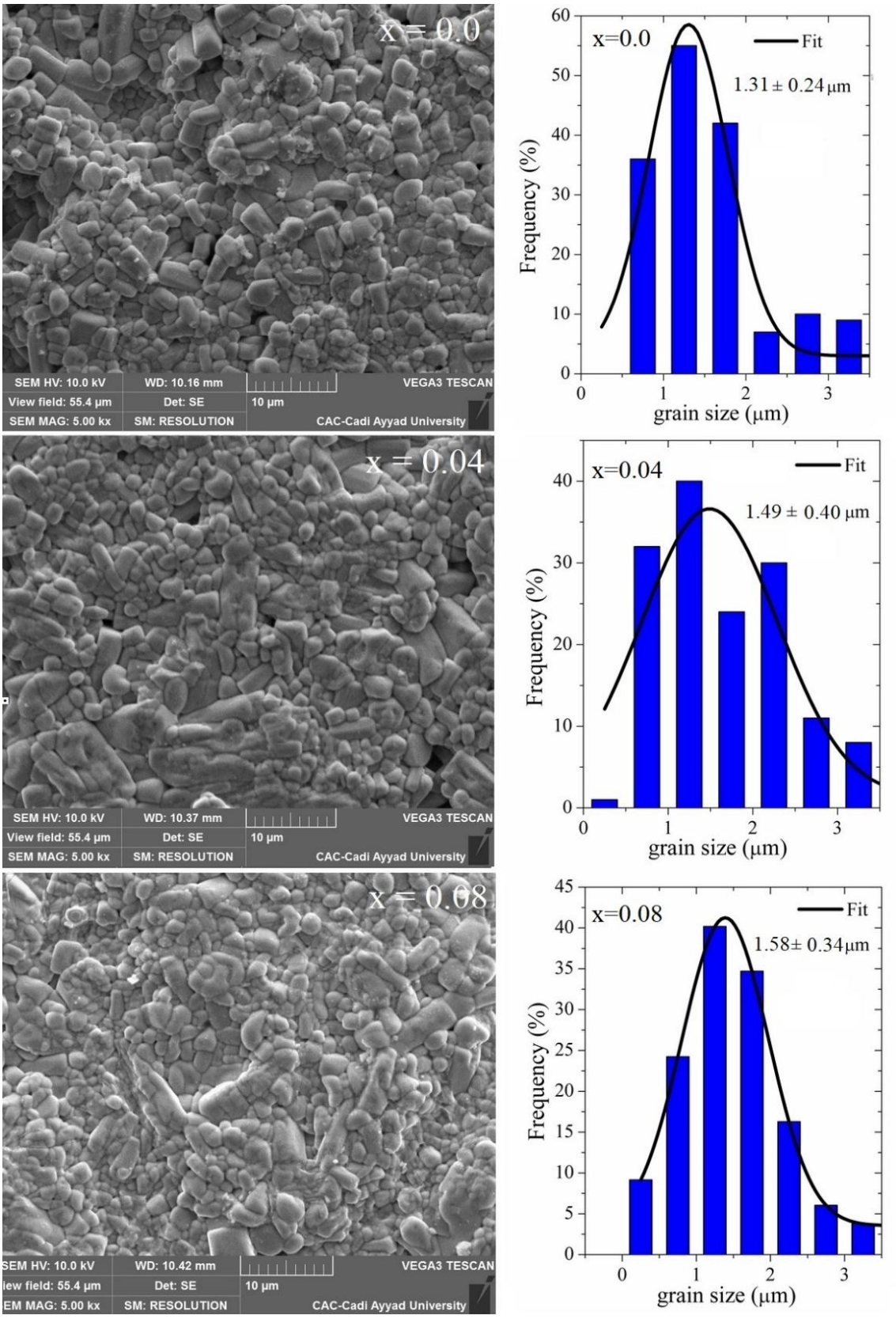

Fig. 8. Scanning electron microscopy images of the $Ba_5CaTi_{2-x}Zn_xNb_8O_{30}$ ceramics (x= 0, 0.04 and 0.08) and associated grain size distributions.

3.3 Study of dielectric properties

The temperature-dependent dielectric constant (ε_r) for $Ba_5CaTi_{2-x}Zn_xNb_8O_{30}$ with (x=0, 0.04, and 0.08) at different frequencies (1 kHz-1 MHz) in the temperature range between 50 and 420 °C is shown in Fig. 9.

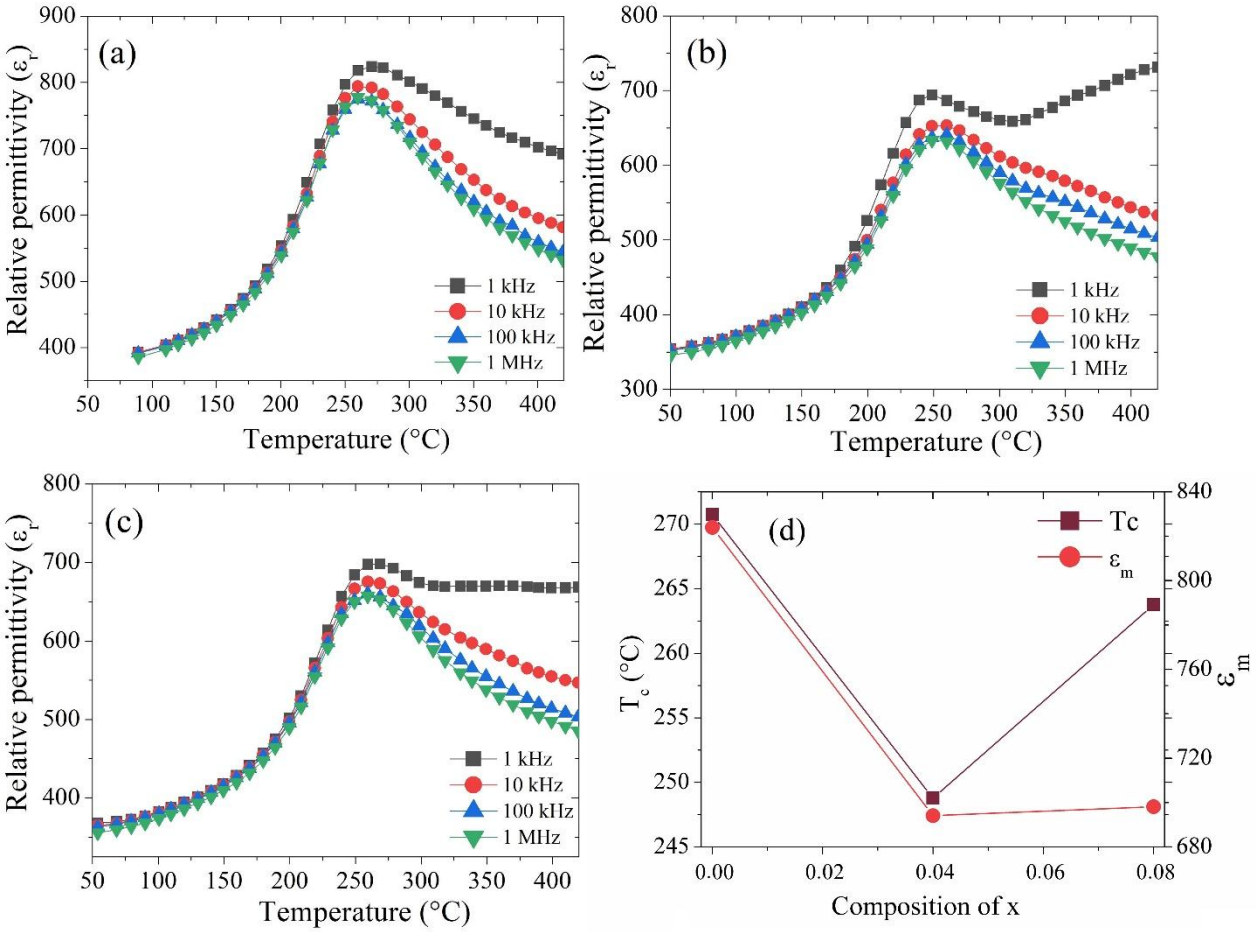

Fig. 9. The temperature and frequency dependencies of dielectric constant for the $Ba_5CaTi_{2-x}Zn_xNb_8O_{30}$ ceramics: (a) 0, (b) 0.04, (c) 0.08, and (d) ε_m and T_C for $Ba_5CaTi_{2-x}Zn_xNb_8O_{30}$ ceramics measured at 1 kHz as a function of x.

Fig. 9 shows the temperature dependence of the dielectric constant for $Ba_5CaTi_{2-x}Zn_xNb_8O_{30}$ ceramics doped with different amounts of ZnO. It can be seen that, for all the obtained ceramics, obvious dielectric peaks were detected. The peaks of ε are associated with the ferroelectric tetragonal phase (P4bm) to paraelectric phase (P4/mbm) transition. It is also observed that the three compounds have the same Curie temperature (T_c) for all frequencies (1kHz-1MHz), indicating that the compounds do not exhibit any relaxor behavior [33]. The dielectric peak is found to be broadened, indicating the existence of a diffuse phase transition. Fig. 9(d) shows the evolution of the dielectric constant and Curie temperature (T_c) for $Ba_5CaTi_{2-x}Zn_xNb_8O_{30}$

ceramics measured at 1 kHz as a function of the rate of Zinc incorporated in the $Ba_5CaTi_{2-x}Zn_xNb_8O_{30}$ structure. With the increase of x, T_c tends to decrease to a value of the order of 248.77°C which corresponds to x=0.04, while the value of dielectric constant for the compound $Ba_5CaTi_2Nb_8O_{30}$ is higher than those of the zinc doped compounds.

This minimum value of T_c for the compound with x=0.04 may be due to the tilting of the oxygen octahedron $Ti/Zn/Nb(2)O_6$ shown in Fig. 7, which reaches a minimum value for Ti(2)-O(5)-Ti(2) and a maximum value for Ti(2)-O(5)-Ti(2) in the compound $Ba_5CaTi_{1.96}Zn_{0.04}Nb_8O_{30}$, or may be due to the high displacement of the cations Ti/Zn/Nb(1) along the c-axis in the compound $Ba_5CaTi_{1.96}Zn_{0.04}Nb_8O_{30}$ in comparison with the other substitutions (Table 4).

The diffuse phase transition behavior of the dielectric constant can be evaluated using the modified Curie - Weiss equation [34, 35].

$$\ln(1/\varepsilon_r - 1/\varepsilon_{rmax}) = \gamma \ln(T - T_{max}) + C_1 \quad (1)$$

Where (ε_r) is the dielectric constant, (ε_{rmax}) is the peak value from ε_r to T_{max}, C_1 is the modified Weiss Curie constant and γ is the diffusivity exponent. The variation of $\ln(1/\varepsilon_r - 1/\varepsilon_{rmax})$ with $\ln(T-T_{max})$ at 1 MHz for $Ba_5CaTi_{2-x}Zn_xNb_8O_{30}$ is shown in Fig. 10. The values from γ obtained from the slope of the curve $\ln(1/\varepsilon_r - 1/\varepsilon_{rmax})$ with $\ln(T-T_{max})$ were 1.75, 1.45, and 1.77 for $Ba_5CaTi_{2-x}Zn_xNb_8O_{30}$ ceramics with (x=0, 0.04, and 0.08) respectively. The value γ is between 1 (normal ferroelectric and obeying Curie-Weiss law) and 2 (relaxing and completely disordered ferroelectric system), implying a diffuse ferroelectric nature of $Ba_5CaTi_{2-x}Zn_xNb_8O_{30}$ ceramics.

The γ value decreases with increasing Zn content, reaches a minimum for x=0.04 and then increases, indicating a decrease in the degree of diffusion of the $Ba_5CaTi_{1.96}Zn_{0.04}Nb_8O_{30}$ ceramics. The diffuse ferroelectric phase transition with a decreasing transition temperature for $Ba_5CaTi_{1.96}Zn_{0.04}Nb_8O_{30}$ ceramics can be seen as a result of the tilting of the oxygen octahedra [36].

We have demonstrated from the results of the structural refinement (Table 2) that we have the formation of oxygen vacancies. Oxygen vacancies (OVs) can easily be formed in oxide materials by the loss of oxygen from the crystal lattice during heating at elevated temperatures (typically >1300 ℃) [37], or in our case by the Ti^{4+}/Zn^{2+} substitution [17]. which using Kröger-Vink notation can be represented as

$$ZnO \xrightarrow{TiO_2} Zn_{Ti}^{//} + O_O^{\times} + V_{\ddot{O}} \quad (2)$$

Where $V_{\ddot{O}}$ denotes oxygen vacancies. The Defects such as oxygen vacancies give rise to disorders in the system, which lead to a diffuse ferroelectric to paraelectric phase transition [38].

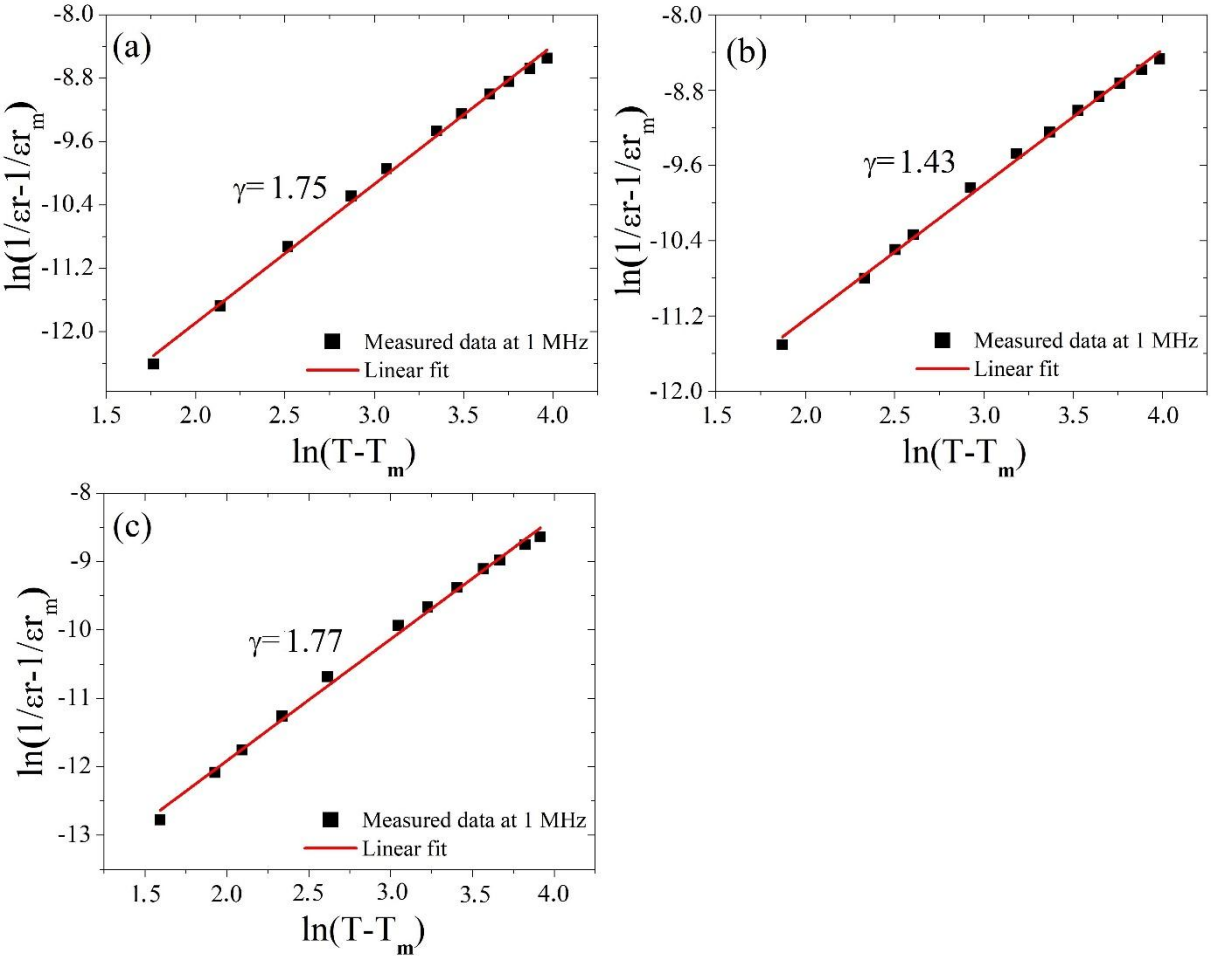

Fig. 10. Plot of ln ($1/\varepsilon_r$-$1/\varepsilon_{rmax}$) as a function of ln ($T - T_{max}$) at 1 MHz for $Ba_5CaTi_{2-x}Zn_xNb_8O_{30}$ ceramic (a) x=0, (b) x=0.04, and (c) x=0.08

Fig. 11(a-d) shows the variation in dielectric loss (tan δ) for $Ba_5CaTi_{2-x}Zn_xNb_8O_{30}$ with (x=0, 0.04, and 0.08) at different frequencies. It can be seen that Fig. 11(a-c) shows a large peak in a temperature range from 200°C to 270°C for $Ba_5CaTi_{2-x}Zn_xNb_8O_{30}$ ceramics. Such a wide maximum in (tan δ) results from the ferroelectric-to-paraelectric phase transition. The dielectric loss peak of ceramics, which appears at a temperature below the dielectric constant, also exhibits a strong frequency dispersion. Fig. 11(d) shows the evolution of the dielectric loss (tan δ) for $Ba_5CaTi_{2-x}Zn_xNb_8O_{30}$ measured at 1 kHz as a function of temperature. It is obviously observed that the dielectric loss (tan δ) of $Ba_5CaTi_{2-x}Zn_xNb_8O_{30}$ ceramics decrease with the

increasing of Zn^{2+} content, which are 0.1165, 0.0734, and 0.048 at 1 kHz, respectively. The incorporation of Zn^{2+} into the Ti^{4+} site reduces the (tan δ) value.

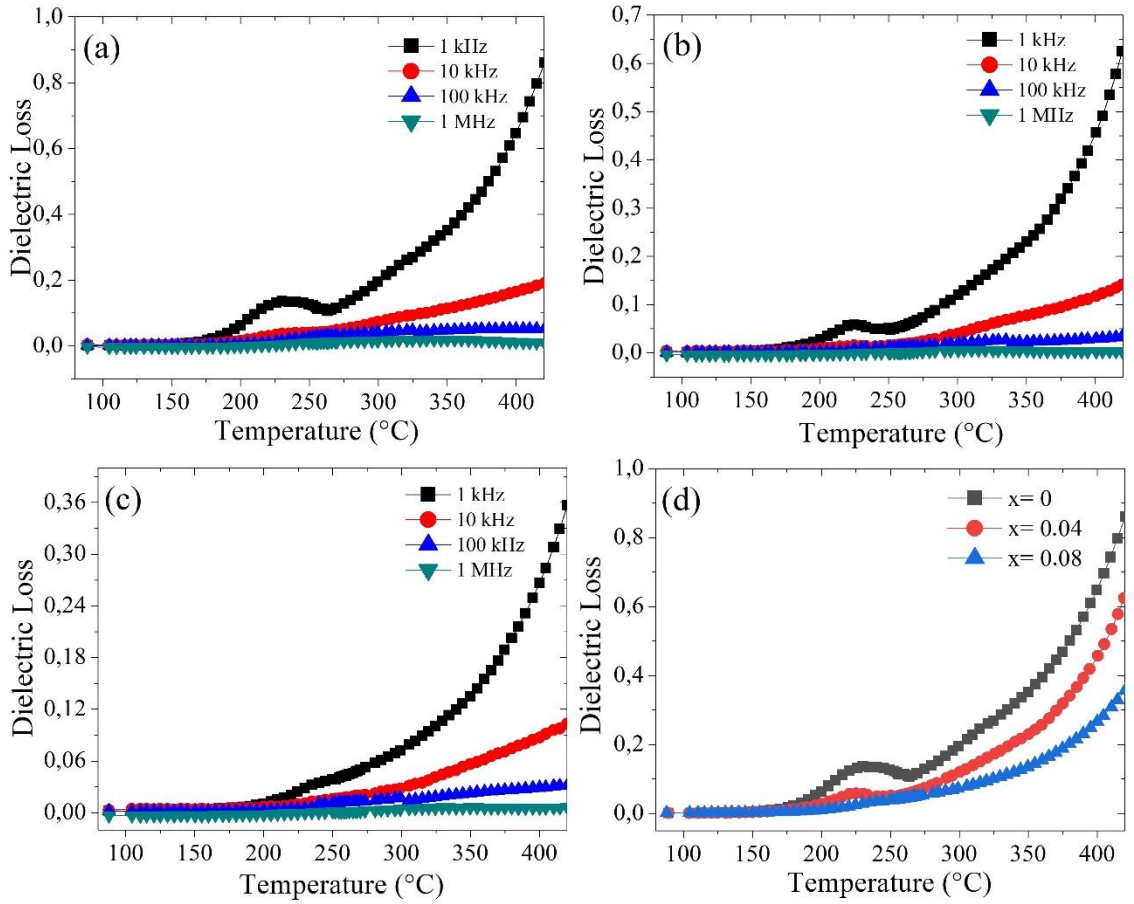

Fig. 11. The temperature and frequency dependencies of dielectric loss for the $Ba_5CaTi_{2-x}Zn_xNb_8O_{30}$ ceramics: (a) 0, (b) 0.04, (c) 0.08, and (d) Dielectric loss for $Ba_5CaTi_{2-x}Zn_xNb_8O_{30}$ ceramics measured at 1 kHz as a function of x.

4. Conclusion

$Ba_5CaTi_{2-x}Zn_xNb_8O_{30}$ ceramics with (x=0, 0.04, and 0.08) were successfully synthesized by the conventional solid-state reaction route. Their structural, and dielectric properties have been systematically studied. Analysis of the XRD data by the Rietveld method showed a tetragonal bronze structure with the space group P4bm and confirmed the formation of oxygen vacancies for all samples. The octahedral distortion changes considerably according to the composition. The off-center displacement of the Ti/Nb/Zn cations along the c-axis is present in both octahedrons $Ti/Zn/Nb(1)O_6$ and $Ti/Zn/Nb(2)O_6$. The octahedrons $Ti/Zn/Nb(1)O_6$ and $Ti/Zn/Nb(2)O_6$ of the $Ba_5CaTi_{2-x}Zn_xNb_8O_{30}$ structure are sensitive to Ti^{4+}/Zn^{2+} substitution, which could contribute to the evolution of the dielectric response within the Ba_5CaTi_{2-}

$_xZn_xNb_8O_{30}$ solid solution. The SEM images show a homogeneous microstructure consisting of unevenly sized grains and minimal porosity. The average grain size is in the range of 1.3 to 1.6 μm. All samples exhibit a diffuse type of ferroelectric-paraelectric phase transition and it shows non-relaxor behaviour. The value of dielectric constant for the compound $Ba_5CaTi_2Nb_8O_{30}$ is significantly higher than those of the zinc doped compounds, the phase change temperature T_c decreases for Zn-doped compounds as compared to undoped compounds and reaches a value of the order of 249°C which corresponds to a x=0.04. The variation of the dielectric loss (tan δ) with temperature shows that (tan δ) decreases with increasing Zn content.

Conflicts of interset

Thre are no conflicts to declare.

Acknowledgments

Department of Chemistry - Multidisciplinary Faculty (FPN), is acknowledged for practical assistance with the recording of the spectral analysis.

References

1. J. Wu, D. Xiao and J. Zhu, *Chemical reviews*, 2015, **115**, 2559-2595.
2. Q. Li, M.-H. Zhang, Z.-X. Zhu, K. Wang, J.-S. Zhou, F.-Z. Yao and J.-F. Li, *Journal of Materials Chemistry C*, 2017, **5**, 549-556.
3. J. F. Li, K. Wang, F. Y. Zhu, L. Q. Cheng and F. Z. Yao, *Journal of the American Ceramic Society*, 2013, **96**, 3677-3696.
4. S. Jindal, A. Vasishth, S. Devi and G. Anand, *Integrated Ferroelectrics*, 2018, **186**, 1-9.
5. B. Yang, S. Hao, P. Yang, L. Wei and Z. Yang, *Ceramics International*, 2018, **44**, 8832-8841.
6. K. Thummavichai, Y. Xia and Y. Zhu, *Progress in Materials Science*, 2017, **88**, 281-324.
7. K. Shimizu, H. Kato, M. Kobayashi and M. Kakihana, *Applied Catalysis B: Environmental*, 2017, **206**, 444-448.
8. P. Botella, B. Solsona, E. García-González, J. M. González-Calbet and J. M. L. Nieto, *Chemical communications*, 2007, 5040-5042.
9. M. Prades, H. Beltrán, N. Masó, E. Cordoncillo and A. R. West, *Journal of Applied Physics*, 2008, **104**, 104118.
10. I. Levin, M. C. Stennett, G. C. Miles, D. I. Woodward, A. R. West and I. M. Reaney, *Applied physics letters*, 2006, **89**, 122908.
11. T. Velayutham, N. Salim, W. Gan and W. A. Majid, *Journal of Alloys and Compounds*, 2016, **666**, 334-340.
12. K. Lin, Y. Rong, H. Wu, Q. Huang, L. You, Y. Ren, L. Fan, J. Chen and X. Xing, *Inorganic chemistry*, 2014, **53**, 9174-9180.
13. Z. J. Yang, W. B. Feng, X. Q. Liu, X. L. Zhu and X. M. Chen, *Journal of the American Ceramic Society*, 2019, **102**, 4721-4729.

14. C. Li, Y. H. Huang, J. S. Hong, X. Q. Liu, J. Li and Y. J. Wu, *Journal of Alloys and Compounds*, 2019, **786**, 126-133.
15. S. Kshirsagar, S. Jigajeni, A. Tarale, D. Salunkhe and P. Joshi, *Journal of Advanced Dielectrics*, 2015, **5**, 1550001.
16. S. Abrahams, P. Jamieson and J. Bernstein, *The Journal of Chemical Physics*, 1971, **54**, 2355-2364.
17. A. Bendahhou, K. Chourti, R. El Bouayadi, S. El Barkany and M. Abou-Salama, *RSC Advances*, 2020, **10**, 28007-28018.
18. E. Garcia-Gonzalez, A. Torres-Pardo, R. Jimenez and J. Gonzalez-Calbet, *Chemistry of materials*, 2007, **19**, 3575-3580.
19. P. Yang, B. Yang, S. Hao, L. Wei and Z. Yang, *Journal of Alloys and Compounds*, 2016, **685**, 175-185.
20. S. Wu, C. Sun, X. Yang, C. Hu, L. Liu and L. Fang, *Ceramics International*, 2020, **46**, 9240-9248.
21. K. Li, X. L. Zhu, X. Q. Liu and X. M. Chen, *Applied Physics Letters*, 2012, **101**, 042906.
22. K. Li, X. Li Zhu, X. Qiang Liu and X. Ming Chen, *Applied Physics Letters*, 2013, **102**, 112912.
23. X. L. Zhu and X. M. Chen, *Journal of the American Ceramic Society*, 2012, **95**, 3185-3191.
24. J. Gardner and F. D. Morrison, *Applied Physics Letters*, 2016, **109**, 072901.
25. M. Stennett, I. Reaney, G. Miles, D. Woodward, A. West, C. Kirk and I. Levin, *Journal of applied physics*, 2007, **101**, 104114.
26. M. Stennett, G. Miles, J. Sharman, I. Reaney and A. West, *Journal of the European Ceramic Society*, 2005, **25**, 2471-2475.
27. N. Karan, R. Katiyar, T. Maiti, R. Guo and A. Bhalla, *Journal of Raman Spectroscopy*, 2009, **40**, 370-375.
28. Y. Yao, C. Zhou, D. Lv, D. Wang, H. Wu, Y. Yang and X. Ren, *Europhysics Letters*, 2012, **98**, 27008.
29. V. Petříček, M. Dušek and L. Palatinus, *Zeitschrift für Kristallographie-Crystalline Materials*, 2014, **229**, 345-352.
30. M. Arshad, H. Du, M. S. Javed, A. Maqsood, I. Ashraf, S. Hussain, W. Ma and H. Ran, *Ceramics International*, 2020, **46**, 2238-2246.
31. P. Fang, H. Fan, Z. Xi, W. Chen, S. Chen, W. Long and X. Li, *Journal of alloys and compounds*, 2013, **550**, 335-338.
32. T. Badapanda, V. Senthil, S. Rout, L. Cavalcante, A. Z. Simões, T. Sinha, S. Panigrahi, M. De Jesus, E. Longo and J. A. Varela, *Current Applied Physics*, 2011, **11**, 1282-1293.
33. P. R. Das, R. Choudhary and B. Samantray, *Journal of alloys and compounds*, 2008, **448**, 32-37.
34. S. M. Pilgrim, A. E. Sutherland and S. R. Winzer, *Journal of the American Ceramic Society*, 1990, **73**, 3122-3125.
35. I. W. Kim, C. W. Ahn, J. S. Kim, T. K. Song, J.-S. Bae, B. C. Choi, J.-H. Jeong and J. S. Lee, *Applied physics letters*, 2002, **80**, 4006-4008.
36. X. Li Zhu, Y. Bai, X. Q. Liu and X. Ming Chen, *Journal of Applied Physics*, 2011, **110**, 114101.
37. U. Balachandran, B. Odekirk and N. Eror, *Journal of Materials Science*, 1982, **17**, 1656-1662.
38. P. Ganguly and A. Jha, *Physica B: Condensed Matter*, 2010, **405**, 3154-3158.